ACSNANO

www.acsnano.org

ARTICLE

Simultaneous Imaging of Dopants and Free Charge Carriers by Monochromated EELS

Hongbin Yang,* Andrea Konečná, Xianghan Xu, Sang-Wook Cheong, Philip E. Batson,* F. Javier García de Abajo,* and Eric Garfunkel

Cite This: *ACS Nano* 2022, 16, 18795−18805

Read Online

ACCESS | Metrics & More | Article Recommendations | Supporting Information

ABSTRACT: Doping inhomogeneities in solids are not uncommon, but their microscopic observation and understanding are limited due to the lack of bulk-sensitive experimental techniques with high enough spatial and spectral resolution. Here, we demonstrate nanoscale imaging of both dopants and free charge carriers in La-doped $BaSnO_3$ (BLSO) using high-resolution electron energy-loss spectroscopy (EELS). By analyzing high- and low-energy excitations in EELS, we reveal chemical and electronic inhomogeneities within a single BLSO nanocrystal. The inhomogeneous doping leads to distinctive localized infrared surface plasmons, including a previously unobserved plasmon mode that is highly confined between high- and low-doping regions. We further quantify the carrier density, effective mass, and dopant activation percentage by EELS and transport measurements on the bulk single crystals of BLSO. These results not only represent a practical approach for studying heterogeneities in solids and understanding structure−property relationships at the nanoscale, but also demonstrate the possibility of infrared plasmon tuning by leveraging nanoscale doping texture.

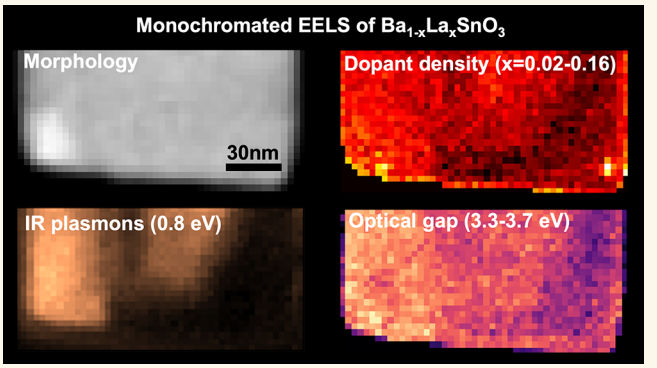

KEYWORDS: *doped semiconductor, high-mobility oxide, infrared plasmonics, band gap, carrier effective mass, monochromated electron energy-loss spectroscopy, inhomogeneity*

The electrical and optical properties of materials are strongly influenced by their free charge carriers.[1] Consequently, tuning the carrier density has been of critical importance for the design and fabrication of semiconductor devices, as well as for exploring exotic electronic states in complex oxides such as superconductivity[2−4] and topological effects.[5] Chemical doping is often exploited to tune the carrier density in solids, although it may introduce chemical and electronic inhomogeneities at the nanoscale.[6−8] These inhomogeneities are often detrimental to carrier mobility and device performance.[9−11] However, in some material systems, the inevitable heterogeneities exhibit a close correlation with the emergence of ferroelectricity,[12−14] high-temperature superconductivity,[15−17] and unconventional magnetism.[18−21]

The relationship between these exotic properties and nanoscale heterogeneities has been challenging to study because of the high demand on both spatial and spectral resolution of the required experimental techniques. Scanning probe microscopy has been useful to cover this gap because it offers the possibility to investigate a wide range of local phenomena, including surface structures and local density of electronic states by scanning tunneling microscopy,[22] nanoscale electrical properties by electrostatic force microscopy,[23,24] and optical excitation strengths by scanning near-field optical microscopy.[25−29] However, the scanning probe techniques are primarily sensitive to surface properties and only offer access to a limited spectral range. Thus, it remains difficult to directly relate the local structure and chemical composition to the electrical or optical properties in materials of interest.[9,30] In this regard, scanning transmission electron microscopy (STEM) combined with electron energy-loss spectroscopy (EELS) represents a powerful alternative, as it allows imaging of atomic structures with the simultaneous measurement of local elemental composition, chemical bonding, and electronic excitations down to the single-atom level.[31]

Received: July 28, 2022
Accepted: October 26, 2022
Published: November 1, 2022

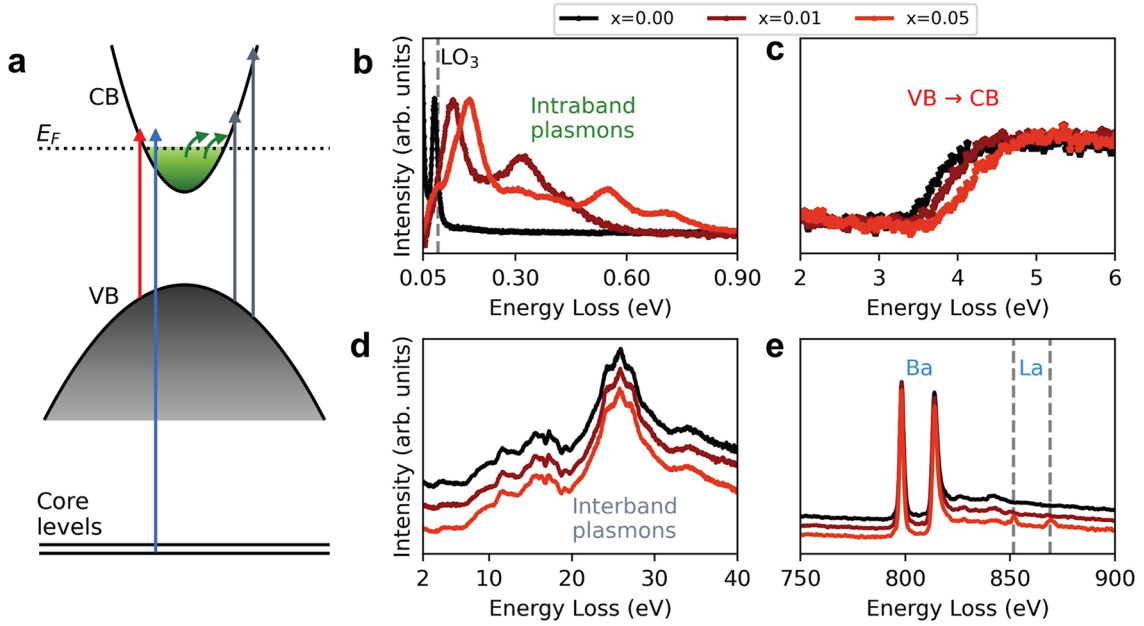

Figure 1. Electronic excitations in EELS. (a) Schematic diagram of electronic excitations, including collective modes (intraband plasmons of free carriers indicated by the green arrows, and interband plasmons indicated by the gray arrows) and single-particle transitions from core levels (blue) or the valence band (VB, red) to the conduction band (CB) states above E_F. (b−e) Doping dependence of low-loss and core-loss EELS in $Ba_{1-x}La_xSnO_3$ single crystals with x = 0, 0.01, and 0.05. (b) Electron energy losses associated with the excitation of phonons and carrier plasmons. The vertical dashed line indicates the highest longitudinal optical phonon energy near 100 meV. (c) Valence to conduction-band-edge transitions. (d) Valence plasmons and higher-energy interband transitions. (e) Core-loss EELS of transitions from Ba and La core levels to unoccupied states. EEL spectra in (d) and (e) are offset for clarity.

Thanks to a series of recent advances in energy resolution,[32,33] state-of-the-art monochromated STEM-EELS provides access into excitations over a broad energy range (from meVs to keVs[34]), thus emerging as the technique of choice to simultaneously probe high-energy core-level transitions and low-energy excitations, such as phonons,[35−43] infrared plasmons,[44−47] and valence electronic excitations.[48,49] Importantly, EELS can be combined with high-resolution imaging[50,51] to reveal local structure−property relationships.

Here, we report a method for characterizing both chemical and electronic inhomogeneities at the nanoscale, demonstrated by a simultaneous imaging of dopants and free charge carriers in La-doped $BaSnO_3$ (BLSO), a high-mobility perovskite oxide.[52−54] Through monochromated STEM-EELS, we measure electronic excitations associated with free carriers and dopants in the low-loss and core-loss regions of EELS, respectively. These measurements and analyses allow for direct imaging of chemical and electronic inhomogeneities, as well as local doping characteristics, even within a single nanocrystal of BLSO. Our results unambiguously show the strong influence of inhomogeneous doping on the plasmonic response. Specifically, we experimentally observe and numerically corroborate an interfacial plasmon mode localized between high- and low-doping regions. We demonstrate inhomogeneous doping as a tool for plasmon customization on the few-nanometer scale, with potential application in the design of advanced devices necessitating a high surface and bulk hybrid confinement of optical fields.

RESULTS AND DISCUSSION

Doping Dependence of Low-Loss and Core-Loss EELS. In EELS, energy-loss events can occur due to different mechanisms, including individual and collective electronic excitations that span a wide energy range, as schematically shown in Figure 1a. The spatial distribution of these excitations can be revealed thanks to the sub-nanometer size of the electron beam traversing the specimen. At relatively high energies, valence plasmons (i.e., collective electronic modes analogous to interband plasmons, but occurring at energies largely exceeding the electronic band gap) and core-losses (single-particle interband transitions involving core electrons to unoccupied states above E_F) are routinely observed in EELS experiments, even at a relatively low energy resolution.[48] Lower-energy excitations in solids, such as phonons and plasmons, as well as interband transitions in the UV−visible spectral range, can be better resolved with the aid of an electron monochromator capable of providing few-meV energy resolution.[32,55]

Here, we observe all of these types of excitations in the bulk single crystals of $Ba_{1-x}La_xSnO_3$ as a function of nominal doping, x, as shown in Figure 1b−e. The crystals were grown by a floating-zone method with homogeneous doping (see Methods). We acquire the EEL spectra in Figure 1 from 5 × 5 nm^2 regions of the TEM specimens. Starting from a wide-band-gap insulator without doping (x = 0), $Ba_{1-x}La_xSnO_3$ becomes a degenerate semiconductor as the level of La doping increases (see x = 0.01, 0.05 curves in Figure 1b,c). The metallic transport properties are manifested in the infrared dielectric response, as revealed in the low-loss region of monochromated EELS in Figure 1b. In the 50−900 meV spectral window, the main processes contributing to electron energy losses are phonons and excitations associated with the doping charge carriers. For undoped crystals, we observe only narrow resonances below ∼90 meV, corresponding to the phonon polaritons in $BaSnO_3$.[56] With increasing n-type doping, the carrier electrons have higher Fermi velocities and

https://doi.org/10.1021/acsnano.2c07540
ACS Nano 2022, 16, 18795−18805

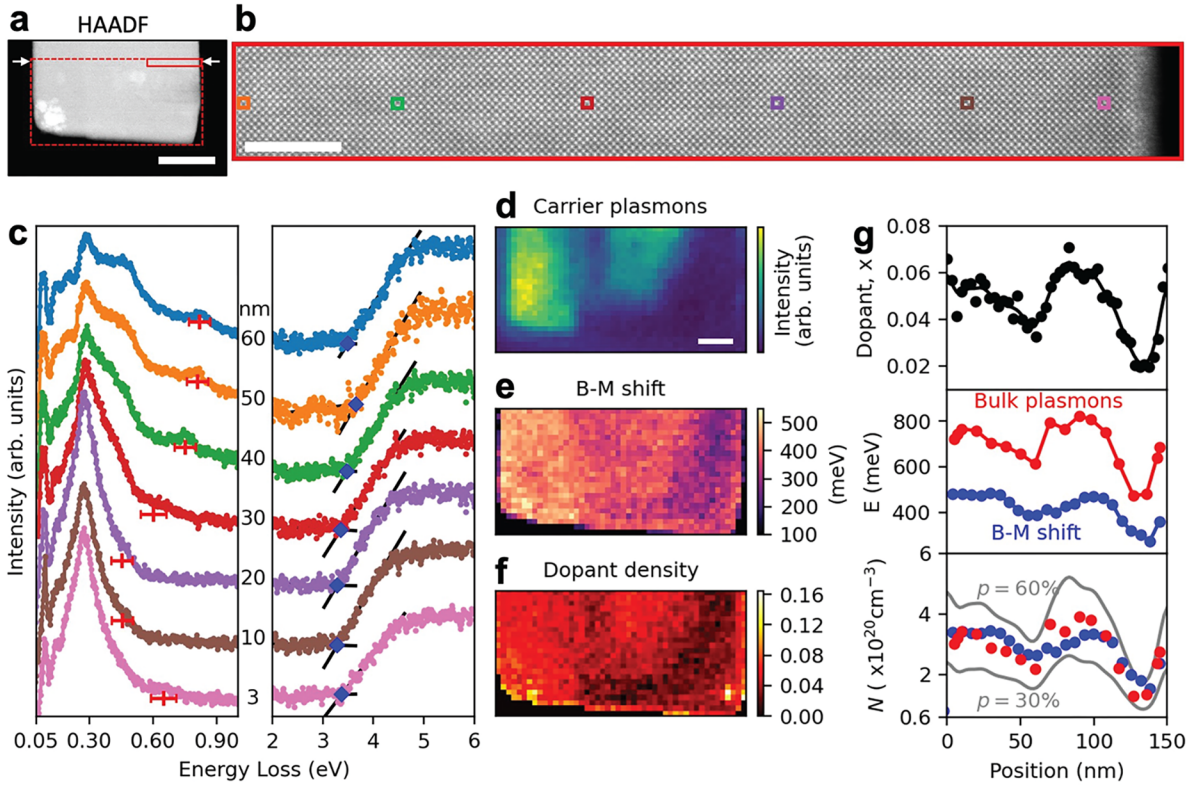

Figure 2. Mapping chemical and electronic inhomogeneities in a BLSO nanocrystal. (a) STEM-HAADF image of a square-shaped BLSO nanocrystal. (b) Atomic-resolution HAADF image near the edge of the crystal, within the rectangular region marked by solid red lines in (a). (c) Low-loss EELS signal acquired at electron beam positions indicated by color-matching squares in the HAADF image in (b). The corresponding distances to the crystal edge are labeled between the two sets of spectra. Spectra at consecutive distances are offset for clarity. The spectrum at 60 nm (blue) is taken outside the region shown in (b). Red and blue markers indicate energies of bulk carrier plasmons and band gaps, respectively. (d) Energy-filtered maps of bulk plasmons integrated from 780 to 830 meV. (e) Burstein−Moss shift map and (f) dopant percentage map for the nanocrystal in (a) over the region indicated by the red dashed rectangle. (g) Dopant percentage (top), bulk carrier plasmon energy and B-M shift (middle), and carrier density (bottom) as a function of electron beam position along a horizontal line between the two white arrows in (a). Gray curves in the bottom panel of (g) indicate doping activation percentages of 30% and 60%. The scale bars in (a), (b), and (d) indicate 50, 5, and 20 nm, respectively.

respond more quickly to the external field than the ions; the phonons are thus screened in doped $BaSnO_3$. The Coulomb interaction between fast electrons and free carriers gives rise to the plasmons that we observe in doped $BaSnO_3$.[57] We refer to these low-energy excitations as carrier plasmons in what follows. As elaborated in later sections, the spectral range of carrier plasmons is primarily set by the carrier density. For the doping level studied here, we observe surface and bulk carrier plasmons below about 1 eV.[58]

Doping-induced changes in the optical band gap, the Burstein−Moss (B-M) shift,[59,60] is also prominent in our EELS measurements over the 2−6 eV energy range shown in Figure 1c. $BaSnO_3$ has a wide band gap of >3 eV[61] and a sufficiently small high-frequency dielectric constant ε_∞ for it to make Cherenkov losses negligible in our EELS experiments with a 60 keV electron beam.[62,63] Although $BaSnO_3$ has a smaller indirect band gap, the associated transition probability is orders of magnitude lower than the direct transitions.[61] Thus, the energy loss intensities we observe here primarily stem from direct interband transitions near the Γ points.[64] The loss signal from indirect transitions likely overlaps with that from defect states from the top and bottom surfaces of the TEM specimen,[65] thus appearing as a nonzero background below the absorption onset dictated by the direct band gap energy. With increasing doping, a blue shift of the optical gap is clearly observed, as shown in Figure 1c.

It should be noted that the carrier plasmons with a strong doping dependence in Figure 1b are intraband in nature. They are accompanied by other more lossy interband plasmons at relatively high energies, whose energy is in fact proportional to the square root of the valence electron density. In view of their origin, we denote these modes as valence plasmons, in contrast to the aforementioned sub-eV carrier plasmons. In the case of undoped $BaSnO_3$, the valence plasmon is around ∼26 eV.[66] In our results, valence plasmons and high-energy interband transitions both show no measurable dependence on doping—we observe nearly identical spectra in undoped and doped crystals (see Figure 1d). This is not unexpected because the lattice constant and valence electronic band structure remain largely unaffected when substituting La for Ba. The introduced carrier density is typically below 1×10^{21} cm^{-3},[67] which is orders of magnitude smaller than the valence electron density and should accordingly cause only marginal variations in the valence plasmons at about 26 eV. Therefore, changes due to carrier doping can be measured exclusively in the low-loss EELS region shown in Figure 1b,c.

We also analyzed core-loss EELS associated with the A-site chemical composition of $BaSnO_3$ (Figure 1e). As expected, the La-$M_{4,5}$ edge intensity increases with nominal doping. For this

https://doi.org/10.1021/acsnano.2c07540
ACS Nano 2022, 16, 18795−18805

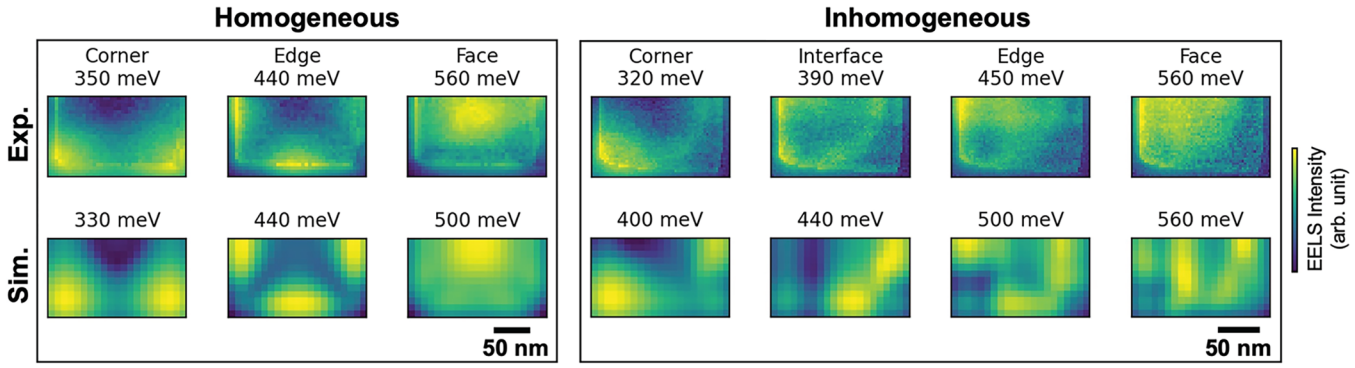

Figure 3. Localized surface plasmons in BLSO nanocrystals. Experimental (top) and simulated (bottom) localized surface plasmons in square-shaped BLSO nanocrystals with homogeneous (left) and inhomogeneous (right) carrier density distributions.

material system and many others, where the dopant and host lattice differ in atomic number by only 1, core-loss EELS is more useful than high-angle annular dark field (HAADF) imaging for identifying dopant locations.

Real-Space Mapping of Dopants and Charge Carrier Excitations. From the knowledge of the excitation energies shown above, dopants and free carriers can be visualized in real space by monochromated EELS mapping. This is demonstrated for a single BLSO nanocrystal, as shown in Figure 2a. This square-shaped BLSO nanoflake is about 20 nm thick as measured by EELS (Section S3, Supporting Information). Although atomic-resolution HAADF imaging of the crystal in Figure 2b shows no substantial contrast variation, low-loss EEL spectra shown in Figure 2c reveal significant changes due to electronic inhomogeneities. From the spectra in the 50−1000 meV energy range, we see how the bulk carrier plasmons are shifting from 830 meV (at a distance of 50 nm from the flake edge) to about 500 meV (20 nm away from the edge). Bulk plasmon energies are signaled by the zero crossing of the frequency-dependent BLSO dielectric function $\varepsilon(\omega)$ (i.e., a pole in the loss function $\mathrm{Im}\{-1/\varepsilon(\omega)\}$). These modes show up as isolated peak maxima in the loss spectra for an electron beam placed at 60, 50, 40, and 3 nm from the flake edge, while they emerge as shoulders of the more intense surface plasmons in the spectra acquired at distances of 30, 20, and 10 nm. This is because, with decreasing energy, the bulk plasmon peaks not only red-shift in energy but also decrease in intensity[68] (Section S1, Supporting Information). In the 200−600 meV spectral range, we observe surface carrier plasmons whose energies are influenced by both the local plasma frequency and the specimen shape, as we show in Figure 3. In addition, we observe phonon polaritons between 80 and 100 meV, whose intensities are inversely proportional to the bulk plasmon energy. We believe the phonon polaritons stem from regions where lattice vibrations are not completely screened by free charge carriers, such as in surface depletion layers.[69,70]

Local optical gaps measured by EELS also show spatial variations, as shown the in 2−6 eV spectra in Figure 2c. We extract the optical gap by modeling the absorption onset (Section S2, Supporting Information) and find that the local optical gap changes between 3.28 and 3.66 eV within the region shown in Figure 2b, depending on the electron beam positions.

Spatial variations of carrier plasmons and optical gap are visualized in the EELS maps in Figure 2d,e for the whole nanocrystal. Figure 2d shows an energy-filtered map of the bulk carrier plasmons in the vicinity of 800 meV. The resonances are observed only in part of the flake (left and center-top), because the rest of the flake shows an $\hbar\omega_p$ value that is considerably lower (Figure 2c and Section S1, Supporting Information). The B-M shift (evaluated with respect to the value obtained for $x = 0$) also shows significant spatial variation, in the range of 200−550 meV. The maps of these two quantities exhibit close correlations, suggesting that the electronic inhomogeneity is a common origin of these variations.

Moreover, we also measure the dopant percentage of this inhomogeneously doped crystal by core-loss EELS mapping, as shown in Figure 2f. The dopant percentage x is defined as $N_{La}/(N_{Ba} + N_{La})$, where N_{Ba} and N_{La} are the numbers of atoms per unit area for Ba and La, respectively. We quantify the dopant percentage from core-loss EELS via the k-factor method, which only requires knowing the ratio of Ba- and La-$M_{4,5}$-edge cross sections, rather than their absolute values.[71] Specifically, we approximate the $M_{4,5}$-edge intensity for Ba and La as N_{Ba} and N_{La}, respectively, and calculate x for each pixel (3.2×3.2 nm^2) of the core-loss EELS map. The result is shown in Figure 2f, where we see that the spatial regions with larger x coincide with regions exhibiting a large B-M shift, as shown in Figure 2e. These regions also feature the high-energy bulk carrier plasmons. Thus, the chemical and electronic heterogeneties are closely related in real space. These spatial variations are also compared more quantitatively as line profiles in Figure 2g, where we plot dopant percentage, the bulk plasmon energy, and the B-M shift as a function of beam position.

Influence of Doping Inhomogeneity on Localized Surface Plasmons. The doping inhomogeneity determined above has a strong influence on the global plasmonic response of the BLSO nanocrystal. This can be seen in a comparison between BLSO nanocrystals with homogeneous and inhomogeneous carrier density distributions, as illustrated in Figure 3. In the left panel of Figure 3, a square-shaped BLSO nanoflake with a relatively homogeneous carrier density distribution shows localized surface plasmon resonances near the corners, edges, and faces at around 350, 440, and 560 meV, respectively. The energy and spatial distribution of these surface plasmons are well reproduced by numerical calculations. Similar geometrically controlled modes are characteristic in cubic-shaped particles, as previously observed in both plasmonic[72−74] and phononic[35,75] materials.

In contrast to homogeneous particles, the BLSO nanocrystals under study, featuring inhomogeneous doping, exhibit substantially different surface plasmon resonances. In the right panel of Figure 3, we visualize the localized surface plasmons of

https://doi.org/10.1021/acsnano.2c07540
ACS Nano 2022, 16, 18795−18805

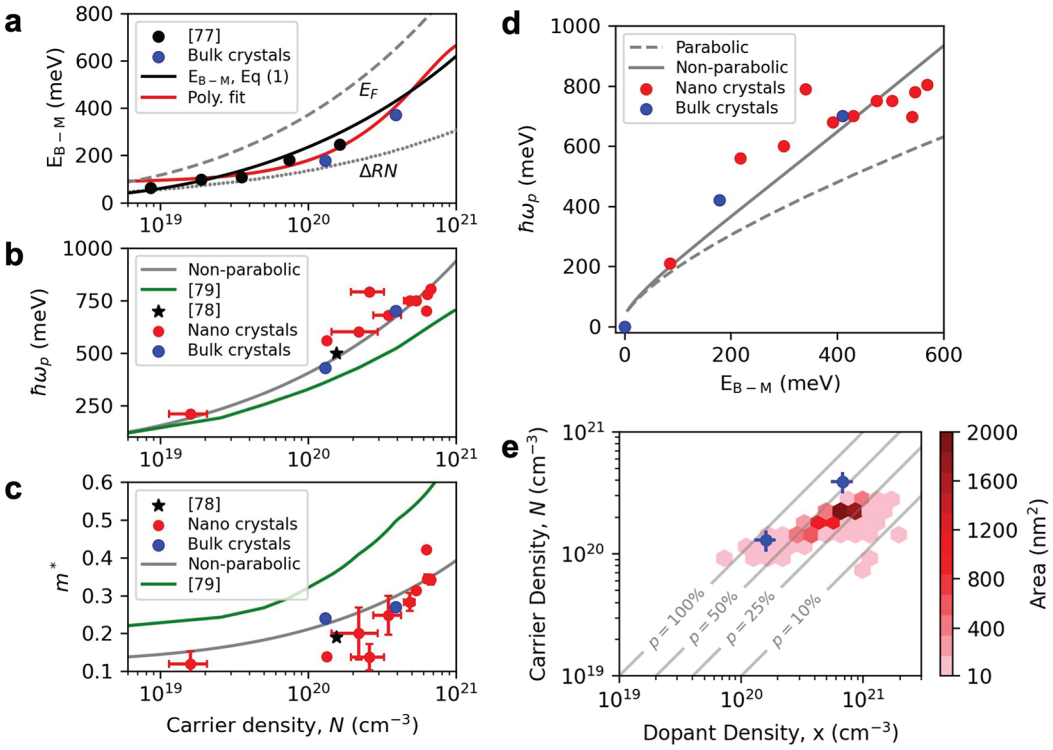

Figure 4. Free carrier characteristics and doping efficiency. Dependence of (a) Burstein−Moss (B-M) shift, (b) bulk plasma frequency, and (c) carrier effective mass on carrier density. Results from refs 77−79 are shown for comparison. (d) Bulk plasmon energy as a function of B-M shift for bulk and nanocrystals as extracted from experiments (symbols), compared with modeled results (gray curves). The red and blue dots represent nano crystals and bulk crystals of BLSO, respectively. (e) Carrier density as a function of dopant density in BLSO. The carrier densities of bulk single crystals are obtained from Hall measurements at room temperature. Carrier and dopant densities of the nanocrystals are extracted from EELS maps in Figure 2. Data points from each pixel (3.2 × 3.2 nm^2) in the EELS maps are represented by hexagons, colored according to the total area for a given N and x.

the BLSO nanoparticle studied in Figure 2. Instead of the existence of corner mode plasmons that brighten all corners at one resonance energy, we observe resonances localized near the left and right corner at different energies. The corner mode at 320 meV only appears near the left corner. The right corner also shows a localized plasmon, but at a much lower energy of ∼180 meV (Section S1, Supporting Information). Although this particle has a size and shape almost identical with that in the left panel of Figure 3, the inhomogeneity in local dopant percentage leads to a different spatially varying carrier density and thus bulk plasma frequency. We corroborate these experimental results through numerical simulations, where we use locally varying bulk plasmon frequencies extracted from experiments. The simulated results also reveal corner modes occurring at different energies as well as similar patterns in energy-filtered maps corresponding to the edge- and face-like plasmons around 450 and 560 meV, respectively. The relatively minor differences between experimental and theoretical results, particularly visible at higher energies, can stem from additional inhomogeneities in plasmon damping, not incorporated in the numerical models. The lower left corner of the flake has a larger thickness (Section S3, Supporting Information), which is the reason plasmon intensities near this location in experiments are higher than the simulated values.

Furthermore, we observe an interesting interfacial plasmon mode in the inhomogeneous nanocrystal. As shown in Figure 3 (right panel), this mode starts to appear near 320 meV, which becomes more pronounced with increasing energy and finally peaks at about 390 meV, before merging with the face-like mode resonance near the high-doping side (above 450 meV in experiments). This interfacial mode forms a circular pattern that is highly confined between the low- and high-doping regions across the whole particle. An interfacial plasmon generally occurs at a boundary that separates two metal-like regions j = 1, 2 that are characterized by different bulk plasma frequencies $\omega_{p,j} \propto \sqrt{N_j/m_j^*}$, dictated in turn by their respective carrier densities N_j and effective masses m_j^*. For a planar interface, the mismatch between the corresponding Drude-like permittivities $(\varepsilon_j(\omega))$; similar to eq S2 in Section S1, Supporting Information) gives rise to a mode signaled by a pole in the Fresnel reflection coefficient. Neglecting retardation, this implies $\varepsilon_1 + \varepsilon_2 = 0$, which leads to the mode frequency $\omega_{12} = \sqrt{(\omega_{p,1}^2 + \omega_{p,2}^2)/(\varepsilon_{\infty,1} + \varepsilon_{\infty,2})}$, where $\varepsilon_{\infty,j}$ are high-frequency dielectric constants. The mode confinement is directly revealed by the EELS probability, which is symmetrically decaying with the distance b to the interface as described by the modified Bessel function $\propto K_0(2\omega_{12}b/v)$, where v is the electron velocity.[48] Although the dopant positions here are random, this phenomenon points to the possibility of infrared plasmon engineering by tuning chemical doping at the atomic scale. For instance, an electromagnetic wave could be guided[76] along an arbitrary path in a low-doping channel with extremely confined size that is determined by the placement of dopants.

Quantifying Free Carrier Characteristics and Doping Efficiency. Next, we quantify the carrier density from the

https://doi.org/10.1021/acsnano.2c07540
ACS Nano 2022, 16, 18795−18805

experimentally measured bulk plasma frequency and optical band gap without making assumptions on the carrier effective mass. The bulk plasma frequency takes the form $\omega_p = \sqrt{Ne^2/\varepsilon_0 m^*}$, where N is the carrier density and m^* the effective mass, e and ε_0 stand for the elementary charge and the vacuum permittivity, respectively. Although the bulk plasma frequency is informative about the infrared and optical properties of materials, it only reveals the ratio between carrier density and effective mass.[80] The carrier effective mass is often highly dependent on doping level because of the band nonparabolicity. Thus, in order to unambiguously determine the carrier density and effective mass from a measurement of $\hbar\omega_p$, knowledge of another doping-dependent quantity is required. In this work, we find that the simultaneous measurement of bulk plasmon loss and the Burstein−Moss shift by EELS makes it possible to quantify both the local carrier density and the effective mass.

In order to corroborate the free carrier density and effective mass quantified from EELS, we have also performed Hall measurements on the bulk single crystals, whose bulk plasmon energy and B-M shift were studied by EELS as shown in Figure 1. The BLSO bulk crystals with x = 0.01, 0.05 have carrier densities $N = 1.3 \times 10^{20}$ and 3.9×10^{20} cm^{-3}, respectively. The results are shown in Figure 4a, together with data from a previous study of BLSO thin films by optical and Hall experiments.[77] We see that the B-M shift increases with carrier density, following a similar trend, although the data are measured with different techniques. The dependence of the B-M shift on carrier density is determined directly from the electronic band structure of $BaSnO_3$. Specifically, the B-M shift can be modeled based on the conduction band structure and doping level as[81]

$$E_{B\text{-}M} = E_F - \Delta_{RN} \tag{1}$$

where E_F is the Fermi energy relative to the conduction band minimum and Δ_{RN} is the gap renormalization due to electron−electron and electron−impurity interactions. More precisely, $\Delta_{RN} = \Delta E_g^{ee} + \Delta E_g^{ei}$, where

$$\Delta E_g^{ee} = \frac{e^2 k_F}{2\pi^2 \varepsilon_s \varepsilon_0} + \frac{e^2 k_{TF}}{8\pi \varepsilon_s \varepsilon_0}\left[1 - \frac{4}{\pi}\tan^{-1}\left(\frac{k_F}{k_{TF}}\right)\right] \tag{2}$$

and

$$\Delta E_g^{ei} = \frac{Ne^2}{\varepsilon_s \varepsilon_0 a_B^* k_{TF}^3} \tag{3}$$

Here, ε_s is the static relative dielectric permittivity, $a_B^* = \frac{\varepsilon_s}{m^*} a_0$ is the effective Bohr radius, a_0 is the Bohr radius, $k_{TF} = \sqrt{\frac{4k_F}{\pi a_B^*}}$ is the Thomas−Fermi screening wave vector, and $k_F = (3\pi N)^{1/3}$ is the Fermi wave vector. Considering a first-order nonparabolic model, the effective mass follows

$$m^* = m^*_{E_F=0}\sqrt{1 + 2\beta\frac{\hbar^2 k^2}{m^*_{E_F=0}}} \tag{4}$$

where $m^*_{E_F=0}$ is the carrier effective mass at the conduction band bottom and β is a parameter describing the band curvature (the increase in m^* with electron wave vector k).

We model the conduction band of $BaSnO_3$ by varying the carrier effective mass, so that the $E_{B\text{-}M}$ values measured at different doping levels can be reproduced by eq 1. Additional material-dependent quantities are the static- and high-frequency dielectric constants, ε_s and ε_∞, which do not change significantly with doping. The results are compared with the experimentally measured $E_{B\text{-}M}$ and N as shown in Figure 4a. Alternatively, a polynomial fit of $E_{B\text{-}M}(N)$ (red curve in Figure 4a) can also provide information on the conduction band curvature. The mean value of the nonparabolic conduction band model and the polynomial fit are shown in Figure 4b,c (solid gray curves). Our best fit to experimental results were found with $m^*_{E_F=0} = 0.12 \pm 0.2$ and $\beta = 1.4$ for the conduction band of $BaSnO_3$.

The electron effective mass in $BaSnO_3$ was found in a wide range in earlier studies, with the smallest value being $m^*_{E_F=0} = 0.06$[82] and most experimental results indicating m^* close to 0.2[78,83,84] for doped $BaSnO_3$. Our results suggest a relatively small m^* at the conduction band bottom and a large nonparabolicity. For N above 1×10^{20} cm^{-3}, our results are in good agreement with the value reported in ref 78, which is obtained from Hall and infrared reflectivity measurements and is widely accepted for $BaSnO_3$. The quick increase of m^* with N we find here is also in line with a recent theoretical study[79] (green curve in Figure 4b,c), where a conduction band inflection point is predicted to exist in $BaSnO_3$ at large Fermi energies.

Given that the B-M shift and the bulk carrier plasmon energy are both dependent on the band curvature, a comparison between the experimental $E_{B\text{-}M}$ and $\hbar\omega_p$ with the modeled values based on the conduction band extracted above serves as a further verification. As shown in Figure 4d, the relation between the B-M shift and the bulk plasma frequency can be described reasonably well with the nonparabolic conduction band model and parameters given above. We note that it should be also possible to extract the conduction band curvature by fitting the relation between the bulk plasmon energy and the B-M shift.

Furthermore, combining the above analysis with core-loss excitations allows us to extract the doping activation percentage p, another important parameter for many material systems,[85−89] which is defined by the ratio between carrier density and dopant concentrations ($p = NV/x$, where V is the unit cell volume). In practice, p is usually evaluated from the ratio between the Hall carrier density and nominal dopant concentration, which is difficult to measure and not well understood at the microscopic level. In BLSO thin films studied earlier, p was found to vary over a wide range, from <10% to ~70%.[83,90−92]

In our study, the Hall carrier densities for the bulk single crystals with x = 0.01, 0.05 correspond to p = 80%, 50%, respectively, as shown in Figure 4e. With the band curvature extracted above, the local carrier density can be calculated from either the B-M shift or the bulk plasma frequency. We use the former in our calculation, as the overlap between bulk and surface carrier plasmons renders the extraction of ω_p less straightforward for low-doping regions. We note that the carrier densities calculated from the B-M shift and the bulk plasma frequency are in good agreement with each other, as shown in the bottom panel of Figure 2g.

Combining the local carrier density with the La percentage shown in Figure 2, we show the activation percentage for the inhomogeneous nanocrystals in Figure 4e, separately measured in 3.2×3.2 nm^2 regions. We observe that the dopant densities

https://doi.org/10.1021/acsnano.2c07540
ACS Nano 2022, 16, 18795−18805

in this nanocrystal vary over a broad range, between 6×10^{19} and 2×10^{21} cm^{-3}, while the carrier densities are centered around 2×10^{20} cm^{-3}. As a result, p for the majority of the regions lies in the range between 25% and 50%. Overall, the dopant activation percentage decreases with doping level for both bulk crystals and nanocrystals of BLSO. The primary source of electron donors are La dopants, as oxygen vacancies are not likely to form in $BaSnO_3$.[93] Thus, the percentage of La dopants that does not contribute to free carriers is rather high, at least 50% for most of the regions. Possible reasons for the incomplete doping activation include charge compensation at surfaces and by defects.[94]

CONCLUSIONS

This study demonstrates the usefulness of low-energy excitations in EELS for understanding the electrical and optical properties at a length scale of a few nanometers. We have shown that the doping-induced changes in the electronic structure can be measured with high spectral and spatial resolution. Changes in the conduction band occupancy should, in principle, also be reflected in near-edge fine structures of core-loss EELS. However, it is impractical to measure such small changes with high accuracy by core-loss EELS (i.e., due to the core−hole lifetime broadening and the small energy loss cross section at high energies). In comparison, low-energy excitations are more sensitive to electronic states near the Fermi level and can be probed with better accuracy. The good agreement between EELS and other experimental methods (Hall measurement, infrared spectroscopy) also supports the validity of the bulk plasma frequency and optical gap measured from monochromated EELS. With a combined analysis of EELS and transport data, it is possible to quantify the local carrier densities and the conduction band curvature. Moreover, combining low-loss and core-loss EELS even allows for a quantification of the doping activation percentage, which otherwise can only be acquired from multiple measurements averaged over large areas. By exploiting the advanced STEM imaging together with monochromated EELS, it should be possible to study local changes in electronic structure down to the individual dopant level.

Our results also suggest that imaging with electronic excitations is not severely limited by inelastic delocalization. It is well-known that higher energy core-loss EELS provides information down to the Ångstrom scale,[95−97] while low-loss EELS often suffers from a poorer spatial localization.[98] Here, we show that both carrier plasmons and band-gap transitions contain information that is sufficiently well localized as to yield useful insight into local optical properties and electronic structure with a resolution of a few nanometers. For example, from the bottom panel of Figure 2g, we see that the carrier density (red and blue dots, obtained via the plasmon energy and B-M shift, respectively) closely tracks the dopant profile (from core loss). This clearly indicates that low-energy excitations are not necessarily more delocalized than high-energy excitations. In our case, carrier electrons in BLSO have an effective Bohr radius of 5−8 nm, which should be the ultimate limit for the attainable spatial resolution.

Quite surprisingly, we have also revealed the existence of a previously unobserved plasmon mode that is highly confined between regions with different doping levels. This finding points to the possibility of engineering a doping profile at the few-nanometer level to guide electromagnetic waves along an arbitrary path, complementary to the geometric control of metallic nanostructures.[99,100] While this approach can be followed over a wide range of length scales depending on the light wavelength and degree of confinement (i.e., in metamaterials operating from the microwave to the visible region), the present analysis relying on BLSO demonstrates a specific example operating in the mid-infrared regime with a high degree of spatial confinement by 2−3 orders of magnitude relative to the light wavelength.

In brief, our work unlocks the full potential of monochromated EELS in providing microscopic insights into the local electronic structure and optical properties, demonstrated here by revealing the electron effective mass, dopant activation percentage, and a heterogeneous-doping-induced interfacial plasmon. These capabilities may lead to exciting discoveries in a wide range of other material systems, where structure−property relationships are of interest.

METHODS

BLSO Crystal Growth and Hall Measurement. The $Ba_{1-x}La_xSnO_3$ nanocrystals were synthesized by the sol−gel method described in ref 58. The nanocrystals studied here have been synthesized with a nominal doping of x = 0.05. The bulk $Ba_{1-x}La_xSnO_3$ crystals were grown by a laser floating-zone technique, for x = 0, 0.01, 0.05. High-purity powders of La_2O_3, $BaCO_3$, and SnO_2 were mixed in the molar ratio $x/2$:1 − x:1.5. La_2O_3 was baked at 900 °C overnight before weighing. The mixed powder was calcined at 1000 °C for 10 h. The product was reground and sintered at 1400 °C for 20 h with one intermediate grinding. The product was reground, filled into a rubber tube, and pressed under 8000 psi hydrostatic pressure. The rod was sintered at 1400 °C for 10 h. The crystals were grown at a rate of 50 mm/h under 8 bar O_2 pressure. The as-grown crystals were annealed at 1400 °C for 20 h in an oxygen flow before measurements.

For Hall measurements, the crystal was oriented, cut, and polished into a (100) plate. The electrodes were made by gold sputtering. The Hall measurements were performed with a Quantum Design PPMS-9 instrument by sweeping the magnetic field at room temperature.

STEM-EELS Experiments. STEM-EELS data were acquired using a Nion Ultra STEM 100 instrument equipped with an electron monochromator. The microscope was operated at 60 kV with a convergence collection half angle of 30 mrad. We set the EELS collection half-angle to 16 mrad when the monochromator was used. In our EELS experiments, the energy resolution and beam current were balanced for each energy range of interest. For phonons and plasmons in the infrared region, a spectrometer dispersion of 1.2 meV/pixel was used to provide the highest possible energy resolution, which is around 10 meV. For band-gap measurements, the spectrometer dispersion was set to 30 meV/pixel to improve the signal-to-noise ratio. This gave a full width at half-maximum of the zero-loss peak (ZLP) of 33 meV. For infrared plasmon and band-gap mapping, the EELS dwell time was set such that the ZLP was just below saturation. This gives 500−800 ms/frame for phonon and plasmon spectra acquisition. For core-loss EELS in the 400−900 eV region, we set the spectrometer dispersion to 300 meV/pixel and did not introduce the monochromator in order to maximize the beam current and thus the signal-to-noise ratio. The EELS dwell time for core-loss spectra acquisition and mapping was set to 2 s/pixel. The point spectra shown in Figures 1 and 2 are integrated over 80−100 frames, with the dwell time mentioned above. Details of EELS data processing are provided in the Supporting Information.

EELS Simulations. We use a finite-element method (as implemented in COMSOL Multiphysics) to calculate the EELS probability for BLSO flakes, with the dielectric function made position-dependent through the spatial distribution of the doping density, as specified in the Supporting Information.

https://doi.org/10.1021/acsnano.2c07540
ACS Nano 2022, 16, 18795−18805

ASSOCIATED CONTENT

Supporting Information

The Supporting Information is available free of charge at https://pubs.acs.org/doi/10.1021/acsnano.2c07540.

EELS data and simulation for phonons and infrared plasmons, band gap analysis from EELS, and low-magnification image and thickness map of the inhomogeneous crystal (PDF)

AUTHOR INFORMATION

Corresponding Authors

Hongbin Yang − *Department of Chemistry and Chemical Biology, Rutgers University, Piscataway, New Jersey 08854, United States;* orcid.org/0000-0002-0098-6944; Email: hongbin.yang@rutgers.edu

Philip E. Batson − *Department of Physics and Astronomy, Rutgers University, Piscataway, New Jersey 08854, United States*; Email: batson@physics.rutgers.edu

F. Javier García de Abajo − *ICFO-Institut de Ciencies Fotoniques, The Barcelona Institute of Science and Technology, 08860 Castelldefels, Barcelona, Spain; ICREA-Institució Catalana de Recerca i Estudis Avançats, 08010 Barcelona, Spain;* orcid.org/0000-0002-4970-4565; Email: javier.garciadeabajo@nanophotonics.es

Authors

Andrea Konečná − *ICFO-Institut de Ciencies Fotoniques, The Barcelona Institute of Science and Technology, 08860 Castelldefels, Barcelona, Spain; Central European Institute of Technology, Brno University of Technology, 61200 Brno, Czech Republic;* orcid.org/0000-0002-7423-5481

Xianghan Xu − *Department of Physics and Astronomy, Rutgers University, Piscataway, New Jersey 08854, United States*

Sang-Wook Cheong − *Department of Physics and Astronomy, Rutgers University, Piscataway, New Jersey 08854, United States*

Eric Garfunkel − *Department of Chemistry and Chemical Biology, Rutgers University, Piscataway, New Jersey 08854, United States; Department of Physics and Astronomy, Rutgers University, Piscataway, New Jersey 08854, United States*

Complete contact information is available at: https://pubs.acs.org/10.1021/acsnano.2c07540

Notes

The authors declare no competing financial interest.

ACKNOWLEDGMENTS

H.Y. and P.E.B. acknowledge financial support of the U.S. Department of Energy, Office of Science, Basic Energy Sciences, under Award No. DESC0005132. X.X. and S.-W.C. were supported by the center for Quantum Materials Synthesis (cQMS), funded by the Gordon and Betty Moore Foundations EPiQS initiative through grant GBMF10104, and by Rutgers University. F.J.G.d.A. acknowledges support by the European Research Council (Advanced Grant 789104-eNANO), the Spanish MICINN (PID2020-112625GB-I00 and Severo Ochoa CEX2019-000910-S), and Fundaciós Cellex and Mir-Puig.

REFERENCES

(1) Zunger, A.; Malyi, O. I. Understanding doping of quantum materials. *Chem. Rev.* **2021**, *121*, 3031−3060.

(2) Ye, J. T.; Zhang, Y. J.; Akashi, R.; Bahramy, M. S.; Arita, R.; Iwasa, Y. Superconducting dome in a gate-tuned band insulator. *Science* **2012**, *338* (6111), 1193.

(3) Edge, J. M.; Kedem, Y.; Aschauer, U.; Spaldin, N. A.; Balatsky, A. V. Quantum critical origin of the superconducting dome in $SrTiO_3$. *Phys. Rev. Lett.* **2015**, *115* (24), 247002.

(4) Li, D.; Wang, B. Y.; Lee, K.; Harvey, S. P.; Osada, M.; Goodge, B. H.; Kourkoutis, L.; Hwang, H. Superconducting dome in $Nd_{1-x}Sr_xNiO_2$ infinite layer films. *Phys. Rev. Lett.* **2020**, *125* (2), 027001.

(5) Hong, S. S.; Cha, J. J.; Kong, D.; Cui, Y. Ultra-low carrier concentration and surface-dominant transport in antimony-doped bi2se3 topological insulator nanoribbons. *Nat. Commun.* **2012**, *3*, 757.

(6) Perea, D. E.; Hemesath, E. R.; Schwalbach, E. J.; Lensch-Falk, J. L.; Voorhees, P. W.; Lauhon, L. J. Direct measurement of dopant distribution in an individual vapour-liquid-solid nanowire. *Nat. Nanotechnol.* **2009**, *4* (5), 315−319.

(7) Koren, E.; Berkovitch, N.; Rosenwaks, Y. Measurement of active dopant distribution and diffusion in individual silicon nanowires. *Nano Lett.* **2010**, *10* (4), 1163−1167.

(8) Ko, W.; Gai, Z.; Puretzky, A. A.; Liang, L.; Berlijn, T.; Hachtel, J. A.; Xiao, K.; Ganesh, P.; Yoon, M.; Li, A.-P. Understanding heterogeneities in quantum materials. *Adv. Mater.* **2022**, 2106909.

(9) Weber, B.; Mahapatra, S.; Ryu, H.; Lee, S.; Fuhrer, A.; Reusch, T. C. G.; Thompson, D. L.; Lee, W. C. T.; Klimeck, G.; Hollenberg, L. C. L.; Simmons, M. Y. Ohmas law survives to the atomic scale. *Science* **2012**, *335* (6064), 64−67.

(10) Jariwala, D.; Krayev, A.; Wong, J.; Robinson, A. E.; Sherrott, M. C.; Wang, S.; Liu, G.-Y.; Terrones, M.; Atwater, H. A. Nanoscale doping heterogeneity in few-layer WSe_2 exfoliated onto noble metals revealed by correlated spm and ters imaging,. *2D Materials* **2018**, *5*, 035003.

(11) Jagadamma, L. K.; Edwards, P. R.; Martin, R. W.; Ruseckas, A.; Samuel, I. D. W. Nanoscale heterogeneity in cspbbr3 and cspbbr3:ki perovskite films revealed by cathodoluminescence hyperspectral imaging. *ACS Applied Energy Materials* **2021**, *4* (3), 2707−2715.

(12) Manley, M. E.; Lynn, J. W.; Abernathy, D. L.; Specht, E. D.; Delaire, O.; Bishop, A. R.; Sahul, R.; Budai, J. D. Phonon localization drives polar nanoregions in a relaxor ferroelectric. *Nat. Commun.* **2014**, *5*, 3683.

(13) Li, F.; Zhang, S.; Yang, T.; Xu, Z.; Zhang, N.; Liu, G.; Wang, J.; Wang, J.; Cheng, Z.; Ye, Z.-G.; Luo, J.; Shrout, T. R.; Chen, L.-Q. The origin of ultrahigh piezoelectricity in relaxor-ferroelectric solid solution crystals,. *Nat. Commun.* **2016**, *7*, 13807.

(14) Kumar, A.; Baker, J. N.; Bowes, P. C.; Cabral, M. J.; Zhang, S.; Dickey, E. C.; Irving, D. L.; LeBeau, J. M. Atomic-resolution electron microscopy of nanoscale local structure in lead-based relaxor ferroelectrics. *Nat. Mater.* **2021**, *20*, 62−67.

(15) Pan, S. H.; O'Neal, J. P.; Badzey, R. L.; Chamon, C.; Ding, H.; Engelbrecht, J. R.; Wang, Z.; Eisaki, H.; Uchida, S.; Gupta, A. K.; Ng, K. W.; Hudson, E. W.; Lang, K. M.; Davis, J. C. Microscopic electronic inhomogeneity in the high-t_c superconductor $Bi_2Sr_2CaCu_2O_{8+x}$. *Nature* **2001**, *413* (6853), 282−285.

(16) Hanaguri, T.; Lupien, C.; Kohsaka, Y.; Lee, D. H.; Azuma, M.; Takano, M.; Takagi, H.; Davis, J. C. A checkerboard electronic crystal state in lightly hole-doped $Ca_{2-x}Na_xCuO_2Cl_2$. *Nature* **2004**, *430* (7003), 1001−1005.

(17) Vershinin, M.; Misra, S.; Ono, S.; Abe, Y.; Ando, Y.; Yazdani, A. Local ordering in the pseudogap state of the high-t_c superconductor $Bi_2Sr_2CaCu_2O_{8+\delta}$. *Science* **2004**, *303* (5666), 1995−1998.

(18) Uehara, M.; Mori, S.; Chen, C. H.; Cheong, S.-W. Percolative phase separation underlies colossal magnetoresistance in mixed-valent manganites. *Nature* **1999**, *399*, 560−563.

(19) Burgy, J.; Mayr, M.; Martin-Mayor, V.; Moreo, A.; Dagotto, E. Colossal effects in transition metal oxides caused by intrinsic inhomogeneities. *Phys. Rev. Lett.* **2001**, *87*, 277202.

(20) Akahoshi, D.; Uchida, M.; Tomioka, Y.; Arima, T.; Matsui, Y.; Tokura, Y. Random potential effect near the bicritical region in perovskite manganites as revealed by comparison with the ordered perovskite analogs. *Phys. Rev. Lett.* **2003**, *90*, 177203.
(21) Dagotto, E. Complexity in strongly correlated electronic systems. *Science* **2005**, *309* (5732), 257−262.
(22) Yin, J.-X.; Pan, S. H.; Zahid Hasan, M. Probing topological quantum matter with scanning tunnelling microscopy. *Nat. Rev. Phys.* **2021**, *3*, 249−263.
(23) Girard, P. Electrostatic force microscopy: principles and some applications to semiconductors. *Nanotechnology* **2001**, *12*, 485−490.
(24) Gramse, G.; Kölker, A.; Škereň, T.; Stock, T. J. Z.; Aeppli, G.; Kienberger, F.; Fuhrer, A.; Curson, N. J. Nanoscale imaging of mobile carriers and trapped charges in delta doped silicon p−n junctions. *Nature Electronics* **2020**, *3*, 531−538.
(25) Johns, R. W.; Bechtel, H. A.; Runnerstrom, E. L.; Agrawal, A.; Lounis, S. D.; Milliron, D. J. Direct observation of narrow mid-infrared plasmon linewidths of single metal oxide nanocrystals. *Nat. Commun.* **2016**, *7*, 11583.
(26) Mooshammer, F.; Sandner, F.; Huber, M. A.; Zizlsperger, M.; Weigand, H.; Plankl, M.; Weyrich, C.; Lanius, M.; Kampmeier, J.; Mussler, G.; Gr-tzmacher, D.; Boland, J. L.; Cocker, T. L.; Huber, R. Nanoscale near-field tomography of surface states on $(Bi_{0.5}Sb_{0.5})_2Te_3$. *Nano Lett.* **2018**, *18* (12), 7515−7523.
(27) Lu, X.; Khatib, O.; Du, X.; Duan, J.; Wei, W.; Liu, X.; Bechtel, H. A.; D'Apuzzo, F.; Yan, M.; Buyanin, A.; Fu, Q.; Chen, J.; Salmeron, M.; Zeng, J.; Raschke, M. B.; Jiang, P.; Bao, X. Nanoimaging of electronic heterogeneity in bi2se3 and sb2te3 nanocrystals. *Advanced Electronic Materials* **2018**, *4* (1), 1700377.
(28) Chen, X.; Hu, D.; Mescall, R.; You, G.; Basov, D. N.; Dai, Q.; Liu, M. Modern scattering-type scanning near-field optical microscopy for advanced material research. *Adv. Mater.* **2019**, *31* (24), 1804774.
(29) Chu, Z.; Zheng, L.; Lai, K. Microwave microscopy and its applications. *Annu. Rev. Mater. Res.* **2020**, *50* (1), 105−130.
(30) Cojocaru, B.; Avram, D.; Kessler, V.; Parvulescu, V.; Seisenbaeva, G.; Tiseanu, C. Nanoscale insights into doping behavior, particle size and surface effects in trivalent metal doped sno2. *Sci. Rep.* **2017**, *7*, 9598.
(31) Zhou, W.; Lee, J.; Nanda, J.; Pantelides, S. T.; Pennycook, S. J.; Idrobo, J. C. Atomically localized plasmon enhancement in monolayer graphene. *Nat. Nanotech* **2012**, *7*, 161−165.
(32) Krivanek, O. L.; Lovejoy, T. C.; Dellby, N.; Aoki, T.; Carpenter, R. W.; Rez, P.; Soignard, E.; Zhu, J.; Batson, P. E.; Lagos, M. J.; Egerton, R. F.; Crozier, P. A. Vibrational spectroscopy in the electron microscope. *Nature* **2014**, *514* (7521), 209−12.
(33) Dellby, N.; Lovejoy, T.; Corbin, G.; Johnson, N.; Hayner, R.; Hoffman, M.; Hrncrik, P.; Plotkin-Swing, B.; Taylor, D.; Krivanek, O.; et al. Ultra-high energy resolution eels,. *Microscopy and Microanalysis* **2020**, *26* (S2), 1804−1805.
(34) Krivanek, O. L.; Dellby, N.; Hachtel, J. A.; Idrobo, J. C.; Hotz, M. T.; Plotkin-Swing, B.; Bacon, N. J.; Bleloch, A. L.; Corbin, G. J.; Hoffman, M. V.; Meyer, C. E.; Lovejoy, T. C. Progress in ultrahigh energy resolution eels. *Ultramicroscopy* **2019**, *203*, 60−67.
(35) Lagos, M. J.; Trugler, A.; Hohenester, U.; Batson, P. E. Mapping vibrational surface and bulk modes in a single nanocube. *Nature* **2017**, *543* (7646), 529−532.
(36) Govyadinov, A. A.; Konečná, A.; Chuvilin, A.; Velez, S.; Dolado, I.; Nikitin, A. Y.; Lopatin, S.; Casanova, F.; Hueso, L. E.; Aizpurua, J.; Hillenbrand, R. Probing low-energy hyperbolic polaritons in van der waals crystals with an electron microscope. *Nat. Commun.* **2017**, *8* (1), 95.
(37) Hage, F. S.; Nicholls, R. J.; Yates, J. R.; McCulloch, D. G.; Lovejoy, T. C.; Dellby, N.; Krivanek, O. L.; Refson, K.; Ramasse, Q. M. Nanoscale momentum-resolved vibrational spectroscopy. *Science Advances* **2018**, *4* (6), eaar7495.
(38) Senga, R.; Suenaga, K.; Barone, P.; Morishita, S.; Mauri, F.; Pichler, T. Position and momentum mapping of vibrations in graphene nanostructures. *Nature* **2019**, *573*, 247−250.
(39) Venkatraman, K.; Levin, B. D. A.; March, K.; Rez, P.; Crozier, P. A. Vibrational spectroscopy at atomic resolution with electron impact scattering. *Nat. Phys.* **2019**, *15*, 1237−1241.
(40) Hage, F. S.; Radtke, G.; Kepaptsoglou, D. M.; Lazzeri, M.; Ramasse, Q. M. Single-atom vibrational spectroscopy in the scanning transmission electron microscope. *Science* **2020**, *367*, 1124−1127.
(41) Yan, X.; Liu, C.; Gadre, C. A.; Gu, L.; Aoki, T.; Lovejoy, T. C.; Dellby, N.; Krivanek, O. L.; Schlom, D. G.; Wu, R.; Pan, X. Single-defect phonons imaged by electron microscopy. *Nature* **2021**, *589* (7840), 65−69.
(42) Konečná, A.; Li, J.; Edgar, J. H.; García de Abajo, F. J.; Hachtel, J. A. Revealing nanoscale confinement effects on hyperbolic phonon polaritons with an electron beam. *Small* **2021**, *17* (39), 2103404.
(43) Li, Y.-H.; Qi, R.-S.; Shi, R.-C.; Hu, J.-N.; Liu, Z.-T.; Sun, Y.-W.; Li, M.-Q.; Li, N.; Song, C.-L.; Wang, L.; Hao, Z.-B.; Luo, Y.; Xue, Q.-K.; Ma, X.-C.; Gao, P. Atomic-scale probing of heterointerface phonon bridges in nitride semiconductor. *Proc. Natl. Acad. Sci. U. S. A.* **2022**, *119* (8), e2117027119.
(44) Granerød, C. S.; Bilden, S. R.; Aarholt, T.; Yao, Y.-F.; Yang, C. C.; Look, D. C.; Vines, L.; Johansen, K. M.; Prytz, O. Direct observation of conduction band plasmons and the related burstein-moss shift in highly doped semiconductors: A STEM-EELS study of Ga−doped ZnO. *Phys. Rev. B* **2018**, *98*, 115301.
(45) Yang, H.; Garfunkel, E. L.; Batson, P. E. Probing free carrier plasmons in doped semiconductors using spatially resolved electron energy loss spectroscopy. *Phys. Rev. B* **2020**, *102* (20), 205427.
(46) Olafsson, A.; Busche, J. A.; Araujo, J. J.; Maiti, A.; Idrobo, J. C.; Gamelin, D. R.; Masiello, D. J.; Camden, J. P. Electron beam infrared nano-ellipsometry of individual indium tin oxide nanocrystals. *Nano Lett.* **2020**, *20* (11), 7987−7994.
(47) Mkhitaryan, V.; March, K.; Tseng, E. N.; Li, X.; Scarabelli, L.; Liz-Marzan, L. M.; Chen, S.-Y.; Tizei, L. H. G.; Stephan, O.; Song, J.-M.; Kociak, M.; García de Abajo, F. J.; Gloter, A. Can copper nanostructures sustain high-quality plasmons? *Nano Lett.* **2021**, *21* (6), 2444−2452.
(48) García de Abajo, F. J. Optical excitations in electron microscopy. *Rev. Mod. Phys.* **2010**, *82*, 209−275.
(49) Tizei, L. H. G.; Lin, Y.-C.; Mukai, M.; Sawada, H.; Lu, A.-Y.; Li, L.-J.; Kimoto, K.; Suenaga, K. Exciton mapping at subwavelength scales in two-dimensional materials. *Phys. Rev. Lett.* **2015**, *114*, 107601.
(50) Voyles, P. M.; Muller, D. A.; Grazul, J. L.; Citrin, P. H.; Gossmann, H. J. L. Atomic-scale imaging of individual dopant atoms and clusters in highly n-type bulk Si. *Nature* **2002**, *416* (6883), 826−829.
(51) Varela, M.; Findlay, S. D.; Lupini, A. R.; Christen, H. M.; Borisevich, A. Y.; Dellby, N.; Krivanek, O. L.; Nellist, P. D.; Oxley, M. P.; Allen, L. J.; Pennycook, S. J. Spectroscopic imaging of single atoms within a bulk solid. *Phys. Rev. Lett.* **2004**, *92* (9), 095502.
(52) Kim, H. J.; Kim, U.; Kim, H. M.; Kim, T. H.; Mun, H. S.; Jeon, B.-G.; Hong, K. T.; Lee, W.-J.; Ju, C.; Kim, K. H.; Char, K. High mobility in a stable transparent perovskite oxide. *Applied Physics Express* **2012**, *5*, 061102.
(53) Raghavan, S.; Schumann, T.; Kim, H.; Zhang, J. Y.; Cain, T. A.; Stemmer, S. High-mobility $BaSnO_3$ grown by oxide molecular beam epitaxy. *APL Materials* **2016**, *4* (1), 016106.
(54) Paik, H.; Chen, Z.; Lochocki, E.; Seidner H, A.; Verma, A.; Tanen, N.; Park, J.; Uchida, M.; Shang, S.; Zhou, B.-C.; Brtzam, M.; Uecker, R.; Liu, Z.-K.; Jena, D.; Shen, K. M.; Muller, D. A.; Schlom, D. G. Adsorption-controlled growth of La-doped $BaSnO_3$ by molecular-beam epitaxy. *APL Materials* **2017**, *5* (11), 116107.
(55) García de Abajo, F. J.; Di Giulio, V. Optical excitations with electron beams: Challenges and opportunities. *ACS Photonics* **2021**, *8* (4), 945−974.
(56) Stanislavchuk, T. N.; Sirenko, A. A.; Litvinchuk, A. P.; Luo, X.; Cheong, S. W. Electronic band structure and optical phonons of $BaSnO_3$ and $Ba_{0.97}Sn_{0.03}O_3$ single crystals: Theory and experiment. *J. Appl. Phys.* **2012**, *112* (4), 044108.

https://doi.org/10.1021/acsnano.2c07540
ACS Nano 2022, 16, 18795−18805

(57) Pines, D.; Bohm, D. A collective description of electron interactions: Ii. collective vs individual particle aspects of the interactions. *Phys. Rev.* **1952**, *85*, 338−353.
(58) Yang, H.; Konečná, A.; Xu, X.; Cheong, S.-W.; Garfunkel, E.; García de Abajo, F. J.; Batson, P. E. Low-loss tunable infrared plasmons in the high-mobility perovskite (Ba,La)SnO_3. *Small* **2022**, *18* (16), 2106897.
(59) Burstein, E. Anomalous optical absorption limit in InSb. *Phys. Rev.* **1954**, *93* (3), 632−633.
(60) Moss, T. S. The interpretation of the properties of indium antimonide. *Proc. Phys. Soc. Sect. B* **1954**, *67* (10), 775−782.
(61) Monserrat, B.; Dreyer, C. E.; Rabe, K. M. Phonon-assisted optical absorption in $BaSnO_3$ from first principles. *Phys. Rev. B* **2018**, *97* (10), 104310.
(62) Chen, C. H.; Silcox, J.; Vincent, R. Electron-energy losses in silicon: Bulk and surface plasmons and Čerenkov radiation. *Phys. Rev. B* **1975**, *12* (1), 64−71.
(63) Stoger-Pollach, M.; Franco, H.; Schattschneider, P.; Lazar, S.; Schaffer, B.; Grogger, W.; Zandbergen, H.W. Cerenkov losses: A limit for bandgap determination and Kramers-Kronig analysis. *Micron* **2006**, *37* (5), 396−402.
(64) Aggoune, W.; Eljarrat, A.; Nabok, D.; Irmscher, K.; Zupancic, M.; Galazka, Z.; Albrecht, M.; Koch, C.; Draxl, C. A consistent picture of excitations in cubic $BaSnO_3$ revealed by combining theory and experiment. *Commun. Mater.* **2022**, *3*, 12.
(65) Rafferty, B.; Brown, L. M. Direct and indirect transitions in the region of the band gap using electron-energy-loss spectroscopy. *Phys. Rev. B* **1998**, *58* (16), 10326−10337.
(66) Yun, H.; Topsakal, M.; Prakash, A.; Ganguly, K.; Leighton, C.; Jalan, B.; Wentzcovitch, R. M.; Mkhoyan, K. A.; Jeong, J. S. Electronic structure of $BaSnO_3$ investigated by high-energy-resolution electron energy-loss spectroscopy and ab initio calculations. *Journal of Vacuum Science and Technology A* **2018**, *36* (3), 031503.
(67) Prakash, A.; Xu, P.; Faghaninia, A.; Shukla, S.; Ager, J. W.; Lo, C. S.; Jalan, B. Wide bandgap $BaSnO_3$ films with room temperature conductivity exceeding 104 S cm^{-1}. *Nat. Commun.* **2017**, *8*, 15167.
(68) Caruso, F.; Verdi, C.; Poncé, S.; Giustino, F. Electron-plasmon and electron-phonon satellites in the angle-resolved photoelectron spectra of n-doped anatase TiO_2. *Phys. Rev. B* **2018**, *97*, 165113.
(69) Chen, Y.; Nannarone, S.; Schaefer, J.; Hermanson, J. C.; Lapeyre, G. J. Coupled plasmon and phonon excitations in the space-charge layer on GaAs (110) surfaces. *Phys. Rev. B* **1989**, *39*, 7653−7658.
(70) Chen, Y.; Hermanson, J. C.; Lapeyre, G. J. Coupled plasmon and phonon in the accumulation layer of InAs (110) cleaved surfaces. *Phys. Rev. B* **1989**, *39*, 12682−12687.
(71) Hofer, F.; Golob, P.; Brunegger, A. EELS quantification of the elements Sr to W by means of $M_{4,5}$ edges. *Ultramicroscopy* **1988**, *25* (1), 81−84.
(72) Sherry, L. J.; Chang, S.-H.; Schatz, G. C.; Van Duyne, R. P.; Wiley, B. J.; Xia, Y. Localized surface plasmon resonance spectroscopy of single silver nanocubes. *Nano Lett.* **2005**, *5* (10), 2034−2038.
(73) Nicoletti, O.; de la Peña, F.; Leary, R. K.; Holland, D. J.; Ducati, C.; Midgley, P. A. Three-dimensional imaging of localized surface plasmon resonances of metal nanoparticles. *Nature* **2013**, *502* (7469), 80−84.
(74) Zhang, S.; Bao, K.; Halas, N. J.; Xu, H.; Nordlander, P. Substrate-induced fano resonances of a plasmonic nanocube: A route to increased-sensitivity localized surface plasmon resonance sensors revealed. *Nano Lett.* **2011**, *11* (4), 1657−1663.
(75) Li, X.; Haberfehlner, G.; Hohenester, U.; Stephan, O.; Kothleitner, G.; Kociak, M. Three-dimensional vectorial imaging of surface phonon polaritons. *Science* **2021**, *371* (6536), 1364.
(76) Law, S.; Roberts, C.; Kilpatrick, T.; Yu, L.; Ribaudo, T.; Shaner, E. A.; Podolskiy, V.; Wasserman, D. All-semiconductor negative-index plasmonic absorbers. *Phys. Rev. Lett.* **2014**, *112*, 017401.
(77) Lebens-Higgins, Z.; Scanlon, D. O.; Paik, H.; Sallis, S.; Nie, Y.; Uchida, M.; Quackenbush, N. F.; Wahila, M. J.; Sterbinsky, G. E.; Arena, D. A.; Woicik, J. C.; Schlom, D. G.; Piper, L. F. Direct observation of electrostatically driven band gap renormalization in a degenerate perovskite transparent conducting oxide. *Phys. Rev. Lett.* **2016**, *116* (2), 027602.
(78) James Allen, S.; Raghavan, S.; Schumann, T.; Law, K.-M.; Stemmer, S. Conduction band edge effective mass of La-doped $BaSnO_3$. *Appl. Phys. Lett.* **2016**, *108* (25), 252107.
(79) Rowberg, A. J. E.; Krishnaswamy, K.; Van de Walle, C. G. Inflection points in the conduction-band structure of $BaSnO_3$. *Phys. Rev. B* **2020**, *102*, 115201.
(80) Franzen, S. Surface plasmon polaritons and screened plasma absorption in indium tin oxide compared to silver and gold. *J. Phys. Chem. C* **2008**, *112* (15), 6027−6032.
(81) Berggren, K. F.; Sernelius, B. E. Band-gap narrowing in heavily doped many-valley semiconductors. *Phys. Rev. B* **1981**, *24*, 1971−1986.
(82) Moreira, E.; Henriques, J.; Azevedo, D.; Caetano, E.; Freire, V.; Albuquerque, E. Structural and electronic properties of $Sr^xBa^{1-x}SnO_3$ from first principles calculations. *J. Solid State Chem.* **2012**, *187*, 186−194.
(83) Kim, H. J.; Kim, U.; Kim, T. H.; Kim, J.; Kim, H. M.; Jeon, B.-G.; Lee, W.-J.; Mun, H. S.; Hong, K. T.; Yu, J.; Char, K.; Kim, K. H. Physical properties of transparent perovskite oxides (Ba,La)SnO_3 with high electrical mobility at room temperature. *Phys. Rev. B* **2012**, *86* (16), 165205.
(84) Niedermeier, C. A.; Rhode, S.; Ide, K.; Hiramatsu, H.; Hosono, H.; Kamiya, T.; Moram, M. A. Electron effective mass and mobility limits in degenerate perovskite stannate $BaSnO_3$. *Phys. Rev. B* **2017**, *95*, 161202.
(85) Capano, M. A.; Ryu, S.; Melloch, M. R.; Cooper, J. A.; Buss, M. R. Dopant activation and surface morphology of ion implanted 4h- and 6h-silicon carbide. *J. Electron. Mater.* **1998**, *27*, 370−376.
(86) Tandon, B.; Ghosh, S.; Milliron, D. J. Dopant selection strategy for high-quality factor localized surface plasmon resonance from doped metal oxide nanocrystals. *Chem. Mater.* **2019**, *31* (18), 7752−7760.
(87) Son, J.; Moetakef, P.; Jalan, B.; Bierwagen, O.; Wright, N. J.; Engel-Herbert, R.; Stemmer, S. Epitaxial srtio3 films with electron mobilities exceeding 30,000 $cm^2V^{-1}s^{-1}$. *Nat. Mater.* **2010**, *9*, 482−484.
(88) Mairoser, T.; Schmehl, A.; Melville, A.; Heeg, T.; Canella, L.; Böni, P.; Zander, W.; Schubert, J.; Shai, D. E.; Monkman, E. J.; Shen, K. M.; Schlom, D. G.; Mannhart, J. Is there an intrinsic limit to the charge-carrier-induced increase of the curie temperature of euo? *Phys. Rev. Lett.* **2010**, *105*, 257206.
(89) Held, R.; Mairoser, T.; Melville, A.; Mundy, J. A.; Holtz, M. E.; Hodash, D.; Wang, Z.; Heron, J. T.; Dacek, S. T.; Holländer, B.; Muller, D. A.; Schlom, D. G. Exploring the intrinsic limit of the charge-carrier-induced increase of the curie temperature of lu- and la-doped euo thin films. *Phys. Rev. Mater.* **2020**, *4*, 104412.
(90) Niedermeier, C. A.; Rhode, S.; Fearn, S.; Ide, K.; Moram, M. A.; Hiramatsu, H.; Hosono, H.; Kamiya, T. Solid phase epitaxial growth of high mobility La:$BaSnO_3$ thin films co-doped with interstitial hydrogen. *Appl. Phys. Lett.* **2016**, *108* (17), 172101.
(91) Singh, P.; Swartz, A.; Lu, D.; Hong, S. S.; Lee, K.; Marshall, A. F.; Nishio, K.; Hikita, Y.; Hwang, H. Y. Large-area crystalline $BaSnO_3$ membranes with high electron mobilities,. *ACS Appl. Electr. Mater.* **2019**, *1* (7), 1269−1274.
(92) Wang, Z.; Paik, H.; Chen, Z.; Muller, D. A.; Schlom, D. G. Epitaxial integration of high-mobility La-doped $BaSnO_3$ thin films with silicon,. *APL Mater.* **2019**, *7* (2), 022520.
(93) Wang, H.; Walter, J.; Ganguly, K.; Yu, B.; Yu, G.; Zhang, Z.; Zhou, H.; Fu, H.; Greven, M.; Leighton, C. Wide-voltage-window reversible control of electronic transport in electrolyte-gated epitaxial $basno_3$. *Phys. Rev. Mater.* **2019**, *3*, 075001.
(94) Scanlon, D. O. Defect engineering of $basno_3$ for high-performance transparent conducting oxide applications. *Phys. Rev. B* **2013**, *87*, 161201.

https://doi.org/10.1021/acsnano.2c07540
ACS Nano 2022, 16, 18795−18805

(95) Batson, P. E. Simultaneous stem imaging and electron energy-loss spectroscopy with atomic-column sensitivity. *Nature* **1993**, *366*, 727−728.
(96) Muller, D. A. Structure and bonding at the atomic scale by scanning transmission electron microscopy. *Nat. Mater.* **2009**, *8*, 263−270.
(97) Botton, G. A.; Lazar, S.; Dwyer, C. Elemental mapping at the atomic scale using low accelerating voltages. *Ultramicroscopy* **2010**, *110* (8), 926−934.
(98) Egerton, R. Scattering delocalization and radiation damage in stem-eels. *Ultramicroscopy* **2017**, *180*, 115−124.
(99) Rossouw, D.; Botton, G. A. Plasmonic response of bent silver nanowires for nanophotonic subwavelength waveguiding. *Phys. Rev. Lett.* **2013**, *110*, 066801.
(100) Raza, S.; Esfandyarpour, M.; Koh, A. L.; Mortensen, N. A.; Brongersma, M. L.; Bozhevolnyi, S. I. Electron energy-loss spectroscopy of branched gap plasmon resonators. *Nat. Commun.* **2016**, *7*, 13790.

https://doi.org/10.1021/acsnano.2c07540
ACS Nano 2022, 16, 18795−18805